# Supporting Information

# Fe-doping induced localized amorphization in ultrathin α-$Ni(OH)_2$ nanomesh for superior oxygen evolution reaction catalysis

*Yanhui Song[a, b], Meixiu Song[a], Peizhi Liu[a], Weiwei Liu[c], Lijun Yuan[c], Xiaodong Hao[d], Linyuan Pei[a], Bingshe Xu[a, d], Junjie Guo[a]*, Ziqi Sun[b,e]**

a Key Laboratory of Interface Science and Engineering in Advanced Materials, Ministry of Education, Taiyuan University of Technology, Taiyuan 030024, P. R. China

b School of Chemistry and Physics, Queensland University of Technology, Brisbane, Queensland 4001, Australia

c College of Materials and Environmental Engineering, Institute for Advanced Magnetic Materials, Hangzhou Dianzi University, Hangzhou 310018, P. R. China

d Materials Institute of Atomic and Molecular Science, Shaanxi University of Science & Technology, Xi'an 710021, P. R. China

e Centre for Materials Science, Queensland University of Technology, Brisbane, Queensland 4001, Australia

Corresponding Author

* E-mail: guojunjie@tyut.edu.cn (J. Guo); ziqi.sun@qut.edu.au (Z. Sun)

## 1. Chemicals and Materials

Iron (III) nitrate nonahydrate ($Fe(NO_3)_3 \cdot 9H_2O$, 98.5 *wt.*%) and nickel (II) nitrate hexahydrate ($Ni(NO_3)_2 \cdot 6H_2O$, 98 *wt.*%) were purchased from Shanghai Macklin Biochemical Co., Ltd. Hexadecyl trimethyl ammonium bromide (CTAB, 99 *wt.*%) was purchased from Aladdin Chemical. Sodium borohydride ($NaBH_4$, 98 *wt.*%) was purchased from Sinopharm Chemical Reagent Co., Ltd. Ruthenium (IV) oxide ($RuO_2$, 99.9 *wt.*%) was purchased from Alfa Aesar. Nafion (5 *wt.*%, DuPont) was purchased from commercial suppliers. Ethanol and potassium hydroxide were purchased from Tianjin Chemical Work in analytic grade (A.R.). All chemicals were used as received without any further purification. Milli-Q ultrapure water (resistance of 18.2 MΩ cm at 25 °C) was used for all experiments.

## 2. Preparation of ultrathin Fe-doped α-$Ni(OH)_2$ nanomeshes

The process of ultrathin Fe-doped α-$Ni(OH)_2$ nanomeshes began with the preparation of two solutions: Solution A containing $Ni(NO_3)_2 \cdot 6H_2O$, $Fe(NO_3)_3 \cdot 9H_2O$ and 0.5 g CTAB in 25 mL water, where the total molar quantity of $Ni(NO_3)_2 \cdot 6H_2O$ and $Fe(NO_3)_3 \cdot 9H_2O$ was kept to be 2.0 mmol, and x/y could be 1/0, 9/1, 5/1, 3/1, 2/1, 1/1. Solution B containing 0.1 g $NaBH_4$ in 10 mL $H_2O$. The solution A was continuously stirred for 0.5 h to completely dissolve the solutes, to which the solution B was added dropwise. After reacting for 5 min, the products were centrifuged and washed with ethanol for five times, and then dried in vacuum at 120 ℃ for 12 h. The elemental ratios of the metals in ultrathin Fe-doped α-$Ni(OH)_2$ nanomeshes were calculated according to their energy-dispersive X-ray spectra; the ratios were found to be similar to the

feeding ratios (**Table S1**, Supporting Information). Therefore, the samples were designated with their feeding ratios, which are α-$Ni(OH)_2$, α-$Ni_{0.9}Fe_{0.1}(OH)_2$, α-$Ni_{0.83}Fe_{0.17}(OH)_2$, α-$Ni_{0.75}Fe_{0.25}(OH)_2$, α-$Ni_{0.67}Fe_{0.33}(OH)_2$ and α-$Ni_{0.5}Fe_{0.5}(OH)_2$, respectively.

### 3. Physical Characterization

Powder X-ray diffraction patterns were recorded on an X-ray diffraction (XRD) with a Rigaku using Cu-Kα radiation with a Ni filter (λ = 1.54059 Å at 10 kV and 10 mA) at a scan rate of 0.05° per second in the 2θ degree range from 5° to 80°. Morphology and structure of the materials were characterized using a SEM/FIB crossbeam workstation (TESCAN, LYRA 3 XMH) operating at an accelerating voltage of 20 kV and a transmission electron microscopy (TEM, JEOL, JEM-2010F) working at an acceleration voltage of 200 kV. The energy dispersive spectroscopy (EDS) was collected using EDS system (Oxford Materials Analysis) equipped on SEM and TEM. The highly annular dark-field (ADF) imaging in an aberration-corrected scanning transmission electron microscope (STEM, JEM-ARM300F (GrandARM)) was used to characterize the atomic structure. Chemical compositions of the synthesized samples and the electrolyte during stability test were examined by ICP-OES (720 ICP-OES, Agilent Technologies). X-ray photoelectron spectroscopy (XPS) measurements were performed to determine the chemical bonding states using an Amicus from 10 kV Mg Kα radiation at the pressure of $1\times10^{-7}$ Par. The BET isotherms were evaluated using a nitrogen adsorption–desorption apparatus (Quadrasorb SI, Quantachrome, USA). BET specific surface area was calculated using adsorption data in a relative pressure range

from P/P0 = 0.05–0.3. Pore size distribution was derived from the adsorption branch using the Barrett-Joyner-Halenda (BJH) method.

The crystallite size of the as-synthesized samples can be estimated using Scherrer's equation[1]

$$D = K\lambda/Bcos(\theta) \quad (1)$$

Where D is the average grain size, K is a shape factor which can be approximated to 0.93, λ is the wavelength of the applied Cu Kα radiation, 0.154056 nm, B is the full width at half-maximum of the diffraction peak (FWHM), and θ is the Bragg angle. When calculating, the FWHM is converted into radian system by the following equation

$$B \times 3.14/180 \quad (2)$$

## 4. Calculation of Amorphous Area Ratio

The amorphous area ratio is calculated with the help of ImageJ. Since there is not much difference between the amorphous area and the surrounding area, it is impossible to use the automatic marquee (Threshold, Analyze Particles, and Color Threshold) and the version of the automatic marquee (Wand Tool and Trainable Weka Segmentation). Therefore, I use the Rectangle and Free Hand Selection Tools to select the amorphous areas and then measure them. The detailed calculation method is as follows:

(1) First, open the picture to be analyzed through FileOpen, and then change the color mode of the picture to 8-bit grayscale through ImageType8-bit.

(2) Next, convert the pixel size (pixels) of the scale in the picture to the actual physical size (nm), then set the conversion relationship through Analyze Set Scale, select "Global", and click OK to complete the setting.

(3) Then, use the rectangle selection tool to select the area of the entire picture, and measure it, and mark it as $\mathbf{A_0}$. Similar, use the Free Hand Selection Tool to select the area of the crystal and nanopore parts, which are denoted as $\mathbf{A_1}$ and $\mathbf{A_2}$, respectively.

(4) Calculate the amorphous area ratio, the specific calculation formula is as follows:

$$Amorphous\ area\ ratio = \left(1 - \frac{A_1}{A_0 - A_2}\right) \times 100\% \quad (3)$$

(5) We selected three different regions for each sample to calculate the amorphous area ratio, then calculate the average and standard deviation.

## 5. Electrochemical Measurements

All the measurements were performed at in a three-compartment electrochemical cell with a CHI 760e electrochemical workstation at room temperature (25 ℃) in 1 M KOH solution for OER. The electrolyte solution was purged with $N_2$ for 30 min before each test. Saturated Calomel Electrode (SCE, filled with saturation KCl solution) and carbon rod (3 mm in diameter) were used as a reference electrode and a counter electrode in all measurements. To prepare the working electrode, 5 mg active catalyst and 5 mg carbon black (Vulcan XC72) were added to 1 mL solution, which containing 475 μL $H_2O$, 475 μL ethanol and 50 μL of 5 *wt.*% Nafion, and sonicated for 30 min. 4.2 μL of this suspension was drop-cast onto a glassy carbon disk electrode (3 mm diameter, 0.071 $cm^2$ area) and left to dry in air, giving a catalyst loading of ~0.296 mg $cm^{-2}$. EIS measurements were conducted under the potential of 1.52 V in the frequency range of 100 kHz to 10 mHz. LSV polarization curves were recorded at a scan rate of 5 mV $s^{-1}$ with 95% iR-compensation unless specifically indicated. I-t curves were recorded at a constant potential of 1.44 without iR-compensation. All potentials

reported in this work were referred to the RHE, which were converted according to the following equation

$$E_{RHE} = E_{SCE} + 0.24 + 0.059 \times pH \quad (4)$$

The overpotential (η) was calculated according to the following formula

$$\eta(V) = E_{RHE} - 1.23V \quad (5)$$

To evaluate the electrochemically active surface areas (ECSA), cyclic voltammetry (CV) was carried out to probe the electrochemical double layer capacitance ($C_{dl}$) of various sample at the non-Faradic region, identified from CV at various scan rates including 2, 5, 10, 15, 20 and 25 mV $s^{-1}$ in the range of 1.16-1.22 V vs. RHE. The capacitance can be calculated by plotting the Δj at 1.19 V vs. RHE in CV against the scan rate[2, 3]. The electrochemical surface area (ECSA, in $cm^2$) of the catalyst is estimated from the $C_{dl}$ according to the following equation[4, 5]

$$ECSA = \frac{C_{dl} \times A}{C_s} \quad (6)$$

In order to exclude the influence of ECSA on the performance comparison, the OER curves were normalized by ECSAs. The ECSA-normalized current density for as prepared catalysts was calculated by

$$Current\ density_{ECSA} = J \times {}^{C_s}/_{C_{dl}} \quad (7)$$

Mass activity ($J_m$, A $g^{-1}$) and turnover frequency (TOF) were evaluated at an overpotential of η=350 mV. The mass activity was calculated from the catalyst loading m (~0.296 mg $cm^{-2}$) and the measured current density J (mA $cm^{-2}$) according to the following equation

$$J_m = J/m \quad (8)$$

Turnover frequency was calculated by Equation (9)

$$TOF = I/(4 \times F \times n) \quad (9)$$

In Equation (6), I is the measured current at a certain overpotential. F is Faraday's constant (96485.3 C $mol^{-1}$), and n is the moles of the total active metal atoms drop-cast on the electrode[6-8].

According to the published literatures[9, 10], for $Ni(OH)_2$, all the Ni atoms were normally regarded as the active sites. However, for other α-$Ni_xFe_y(OH)_2$, all the Fe atoms are assumed to be accessible for catalyzing the OER. Herein, n is the amount of loaded Ni or Fe atoms which could be calculated from the ICP-OES results (**Table S1**) in this work.

## 6. Density functional theory (DFT) calculations

Calculations were performed by using periodic, spin-polarized DFT as implemented in Vienna ab initio program package (VASP) code, with a 1x2x1 k-point Monkhorst-Pack mesh for the first Brilliouin Zone and plane wave basic set with the kinetics cutoff energy of 400 eV. The periodic condition is employed along the y direction. All atoms in the supercell are allowed to relax during the structure optimization. The relaxation is stopped when the force residue on the atom is smaller than 0.02 eV/Å. The vacuum space along the z direction was set to be 15 Å. Hubbard-U correction (DFT+U method) was applied to improve the description of localized Ni d-electrons in the LDH. A value of U = 6.0 eV was set. A Single layer slab (containing 88 atoms) with (33-5) surface cleavage as the active surface was modeled (see **Fig.**

**S18**). For Fe doped α-$Ni(OH)_2$, one surface Ni atom was substituted by Fe. Based on OER mechanism in alkaline conditions, the free energy of three intermediate states, *OH, *O, and OOH*, are important to identify a given material's OER activity.

The binding energies of the intermediates $O^*$, $OH^*$ and OOH* were calculated with the following equations:

$$\Delta E_{O*} = E(O*) - E(*) - (E_{H_2O} - E_{H_2}) \quad (10)$$

$$\Delta E_{OH*} = E(OH*) - E(*) - (E_{H_2O} - 1/2E_{H_2}) \quad (11)$$

$$\Delta E_{OOH*} = E(OOH*) - E(*) - (2E_{H_2O} - 3/2E_{H_2}) \quad (12)$$

where $E$(O*), $E$(OH*), and $E$(OOH*) are the energies of the clean surface and the surfaces with O*, OH*and OOH* adsorbed, respectively. $E_{H_2O}$ and $E_{H_2}$ are the calculated energies of $H_2O$ and $H_2$ molecules in the gas phase.

The adsorption free energy (ΔGads) is obtained by

$$\Delta G_{ads} = \Delta E_{ads} + \Delta ZPE - T\Delta S \quad (13)$$

Where $\Delta ZPE$ and $\Delta S$ are t zero point energy change and entropy change of the intermediate adsorbed, respectively. The values of $\Delta ZPE$ and $\Delta S$ of the related intermediates are obtained in the former work of Norskov.

The Gibbs free energy change for steps 1-4 can be expressed as

$$\Delta G_1 = \Delta G_{OH} - eU \quad (14)$$

$$\Delta G_2 = \Delta G_O - \Delta G_{OH} - eU \quad (15)$$

$$\Delta G_3 = \Delta G_{OOH} - \Delta G_O - eU \quad (16)$$

$$\Delta G_4 = 4.92[eV] - \Delta G_{OOH} - eU \quad (17)$$

where U is the potential measured against normal hydrogen electrode (NHE) at standard conditions.

The theoretical overpotential ($\eta_{the}$) at standard conditions is given by the equation below:

$$\eta_{OER} = \{\max[(\Delta G^0_{O*} - \Delta G^0_{OH*}), 3.2\ eV] - (\Delta G^0_{O*} - \Delta G^0_{OH*})/e\} - 1.23\ V \quad (18)$$

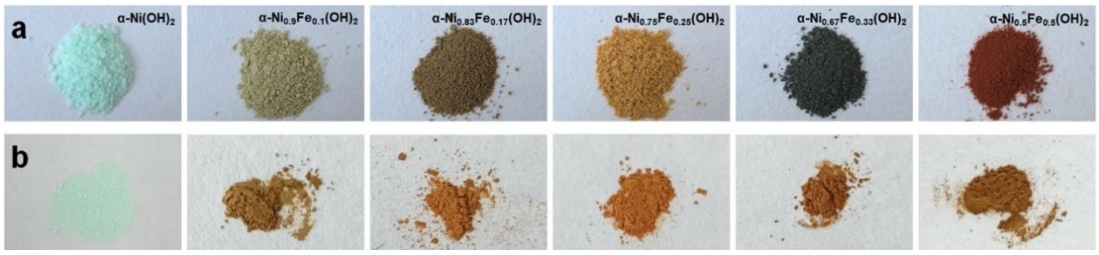


**Fig. S1**. Photographic images of (a) Fe-doped $Ni(OH)_2$ fabricated with different doping contents, (b) physical mixing of $Fe(OH)_3$ with $Ni(OH)_2$ with the same compositions.

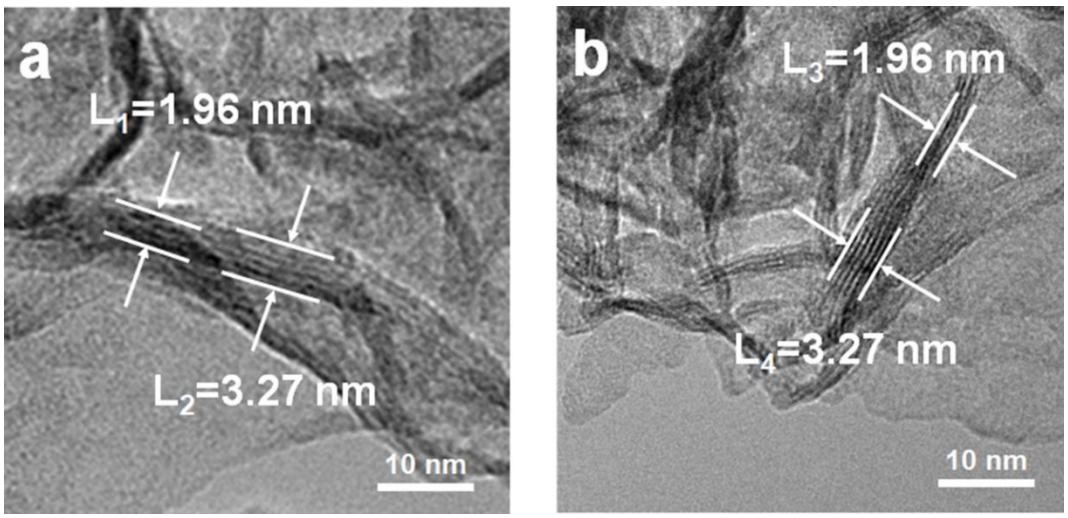


**Fig. S2.** (a) Thickness of α-$Ni(OH)_2$ as observed by TEM, showing the 3~5-layer stacking of α-$Ni(OH)_2$. (b) Thickness of α-$Ni_{0.75}Fe_{0.25}(OH)_2$ as observed by TEM, showing the 3~5-layer stacking of α-$Ni_{0.75}Fe_{0.25}(OH)_2$.

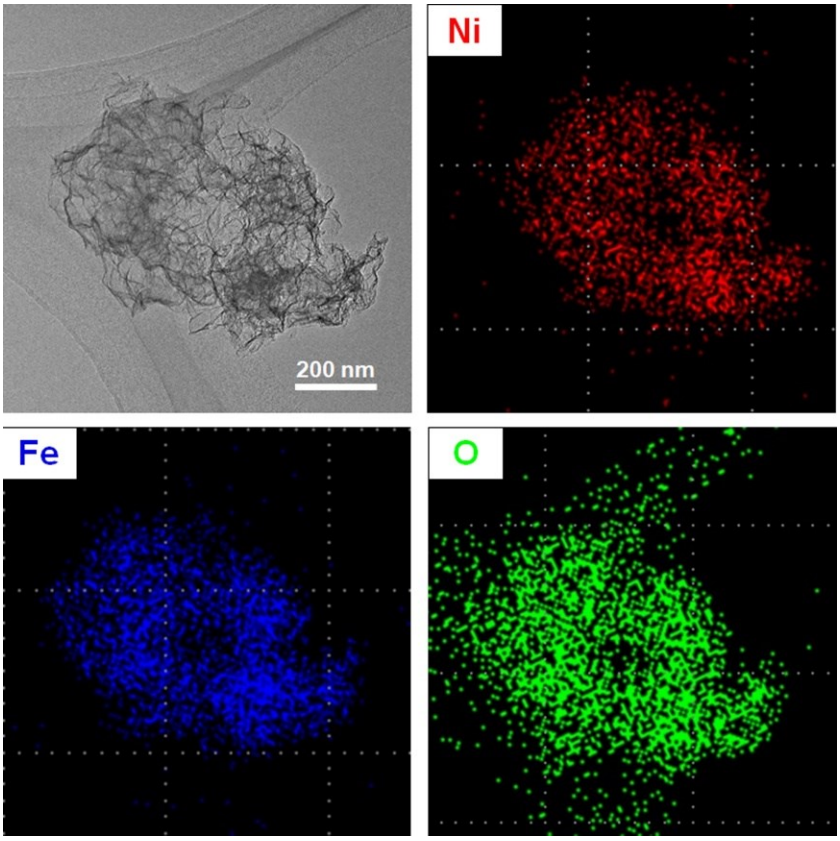


**Fig. S3.** EDS mapping images of α-$Ni_{0.75}Fe_{0.25}(OH)_2$.

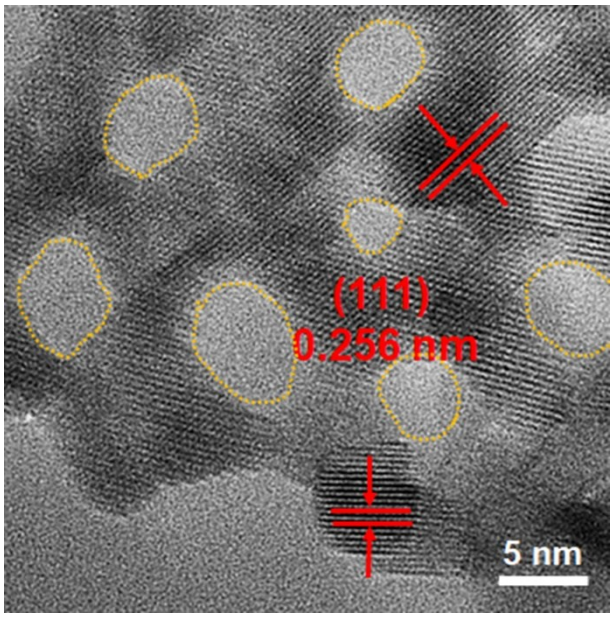


**Fig. S4.** HRTEM image of α-$Ni(OH)_2$. Yellow dotted lines show nanopores.

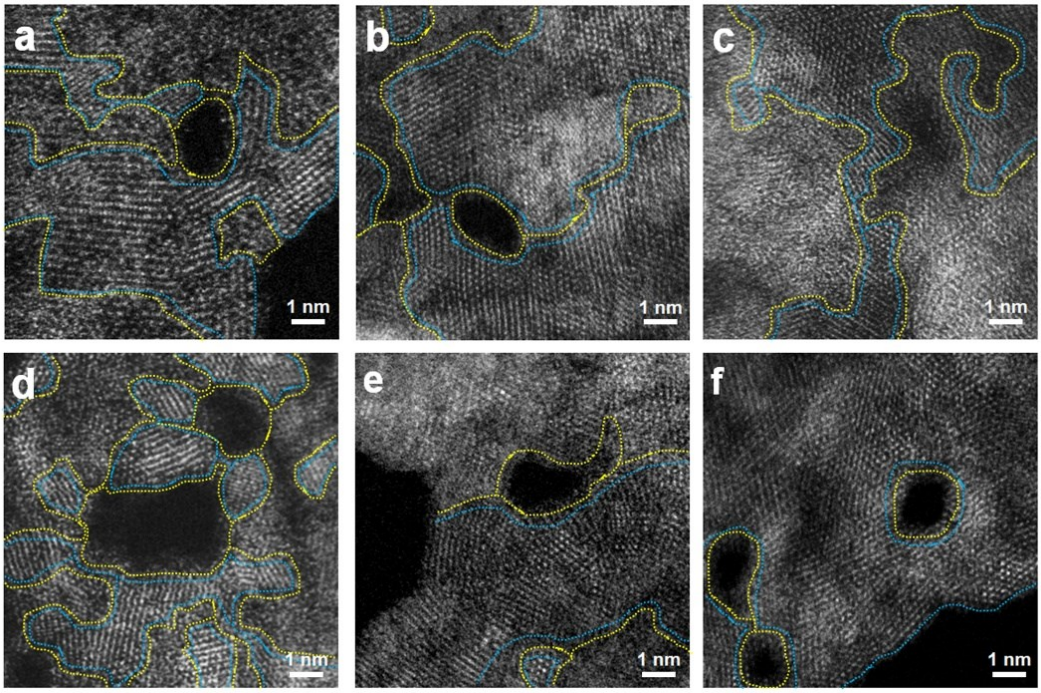


**Fig. S5.** HAADF-STEM images of (a) α-$Ni(OH)_2$, (b) α-$Ni_{0.9}Fe_{0.1}(OH)_2$, (c) α-$Ni_{0.83}Fe_{0.17}(OH)_2$, (d) α-$Ni_{0.75}Fe_{0.25}(OH)_2$, (e) α-$Ni_{0.67}Fe_{0.33}(OH)_2$, and (f) α-$Ni_{0.5}Fe_{0.5}(OH)_2$, respectively. Yellow dotted lines show nanopores and amorphous regions. Blue dotted lines show crystalline regions

.

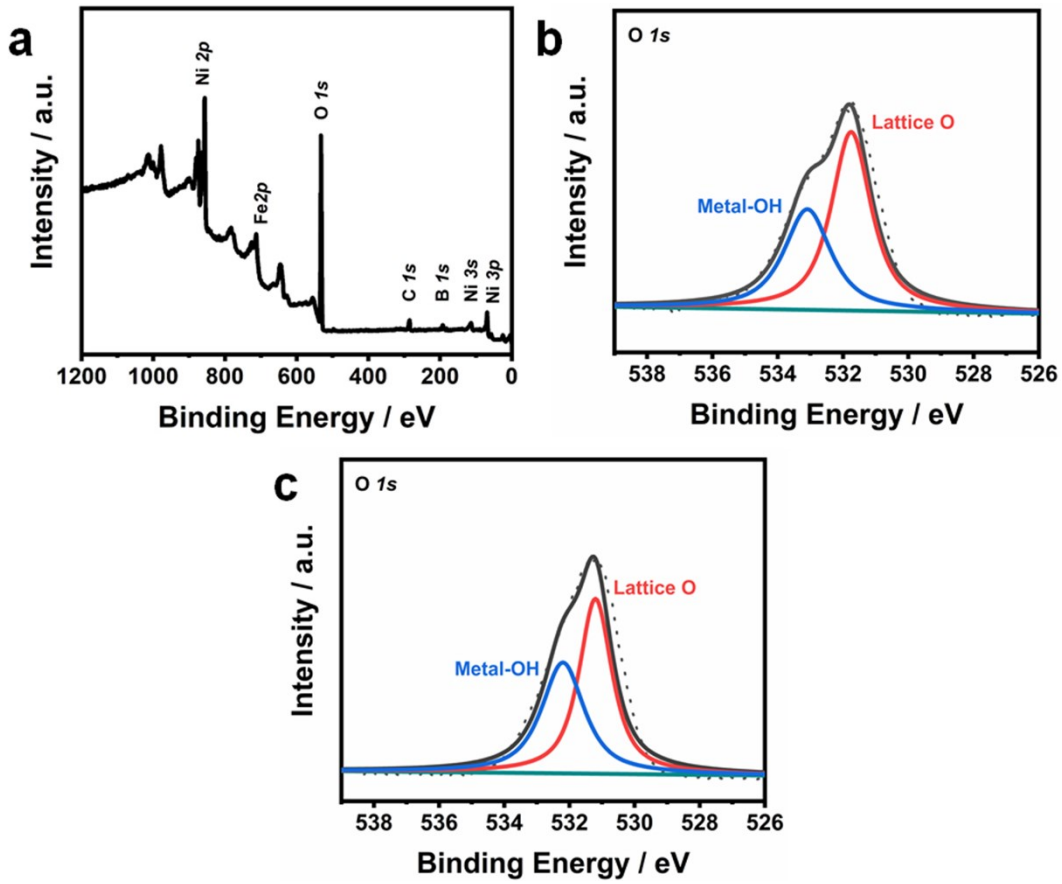


**Fig. S6. (**a) XPS survey spectrum of α-$Ni_{0.75}Fe_{0.25}(OH)_2$. (b) O *1s* XPS spectra of α-$Ni_{0.75}Fe_{0.25}(OH)_2$. (c) O *1s* XPS spectra of α-$Ni(OH)_2$.

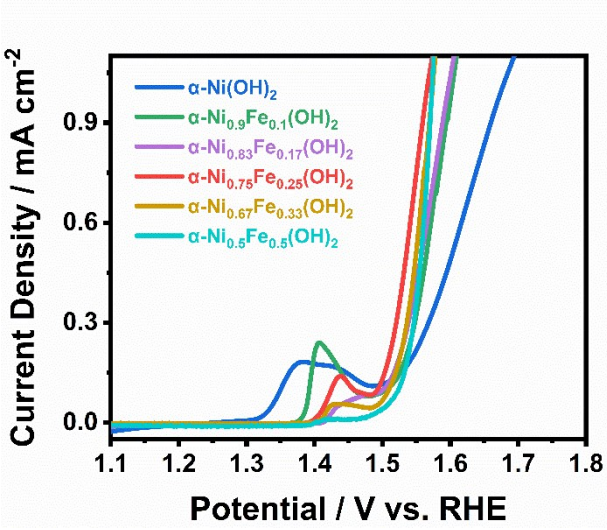


**Fig. S7.** ECSA-normalized LSV curves.

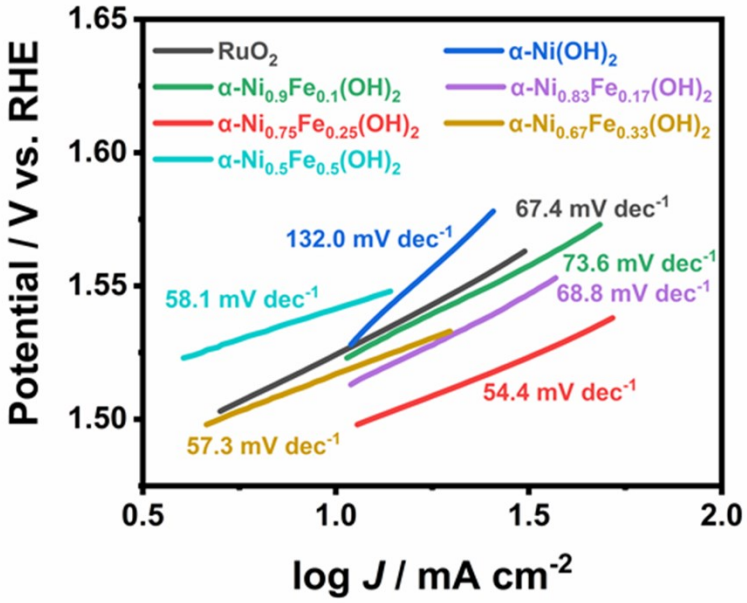


**Fig. S8.** Tafel plots derived from **Figure 4a**.

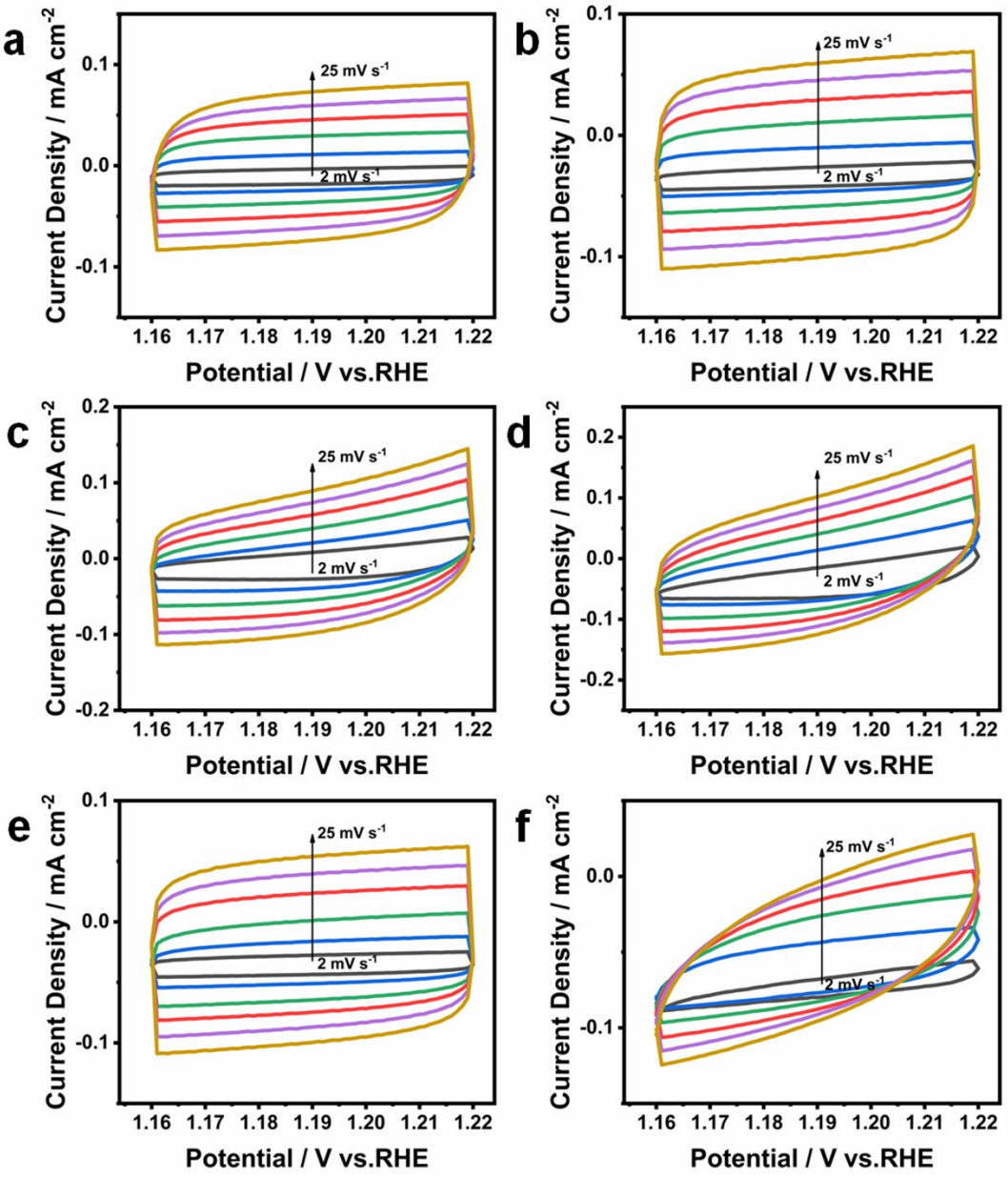


**Fig. S9.** The CVs of (a) α-$Ni(OH)_2$, (b) α-$Ni_{0.9}Fe_{0.1}(OH)_2$, (c) α-$Ni_{0.83}Fe_{0.17}(OH)_2$, (d) α-$Ni_{0.75}Fe_{0.25}(OH)_2$, (e) α-$Ni_{0.67}Fe_{0.33}(OH)_2$, and (f) α-$Ni_{0.5}Fe_{0.5}(OH)_2$ at different scan rates of 2, 5, 10, 15, 20 and 25 mV $s^{-1}$.

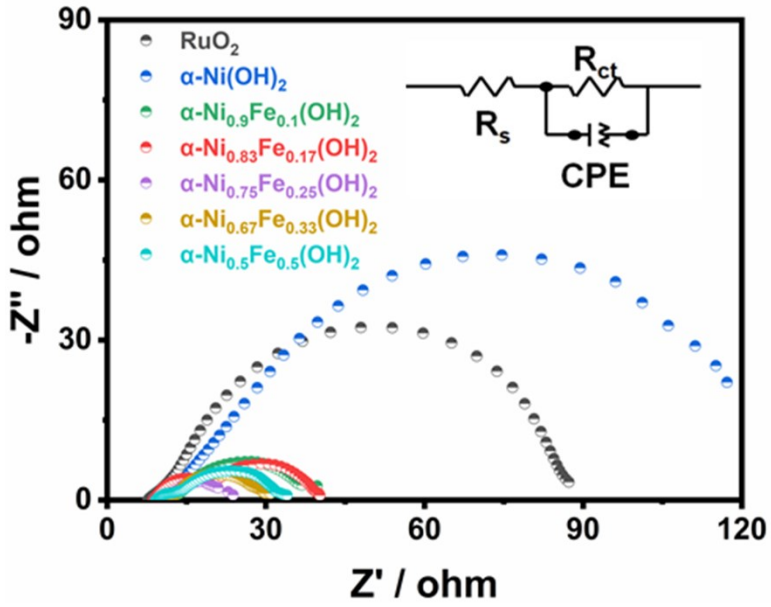


**Fig. S10.** Nyquist plots of $RuO_2$, α-$Ni(OH)_2$, α-$Ni_{0.9}Fe_{0.1}(OH)_2$, α-$Ni_{0.83}Fe_{0.17}(OH)_2$, α-$Ni_{0.75}Fe_{0.25}(OH)_2$, α-$Ni_{0.67}Fe_{0.33}(OH)_2$, and α-$Ni_{0.5}Fe_{0.5}(OH)_2$ in 1 M KOH electrolyte at a overpotential of 350 mV.

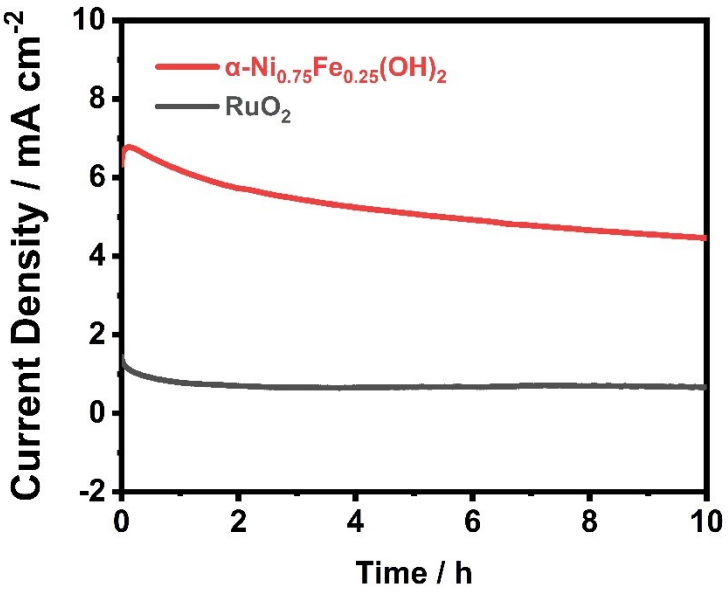


**Fig. S11.** Chronoamperometric (I-t) curves (η = 280 mV) of different catalysts for OER.

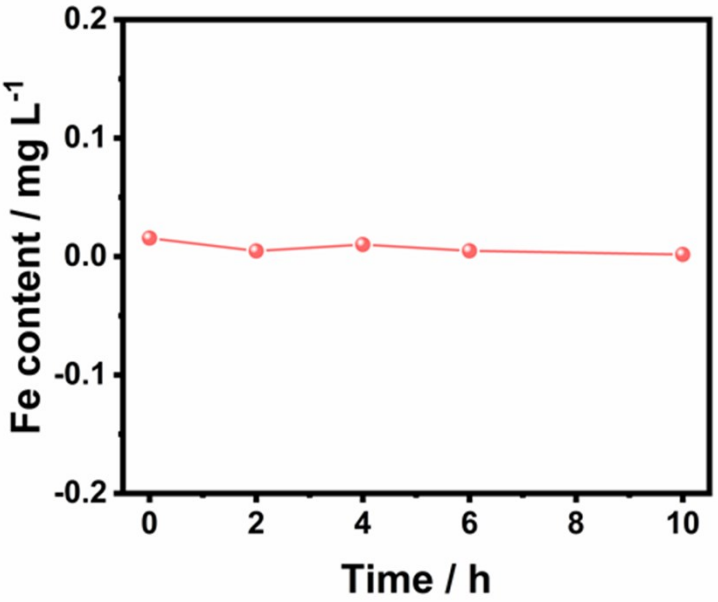


**Fig. S12**. Fe content in the electrolyte during the stability test.

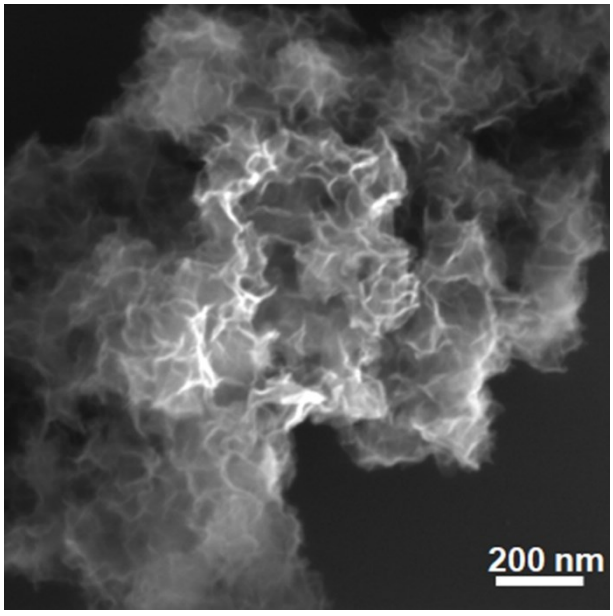


**Fig. S13**. SEM image for α-$Ni_{0.75}Fe_{0.25}(OH)_2$ after OER stability test.

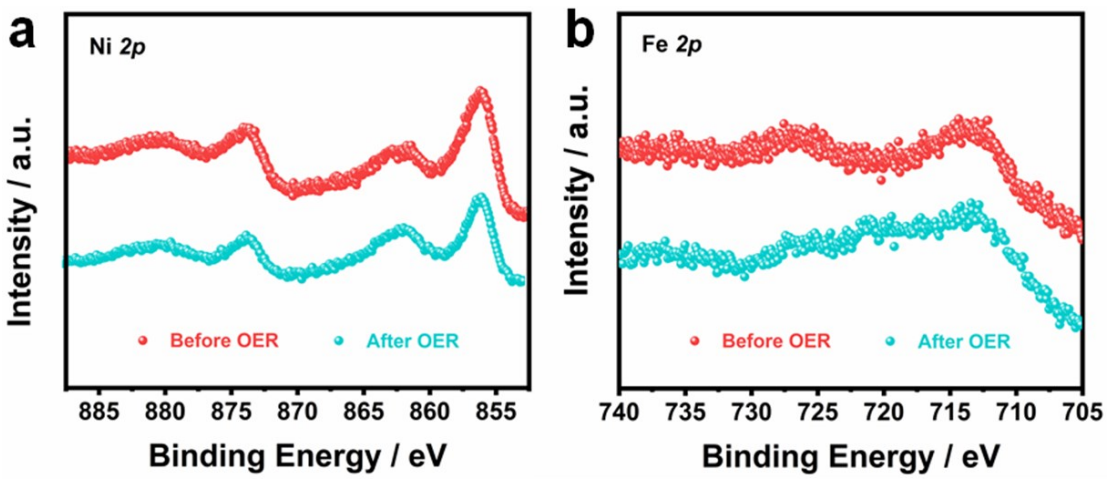


**Figure S14.** Ni *2p* and Fe *2p* XPS spectra of α-$Ni_{0.75}Fe_{0.25}(OH)_2$ before and after OER stability test.

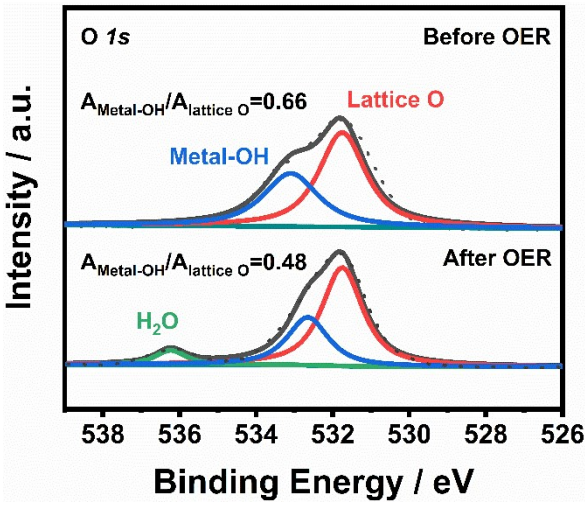


**Figure S15.** O *1s* XPS spectra of α-$Ni_{0.75}Fe_{0.25}(OH)_2$ before and after OER stability test.

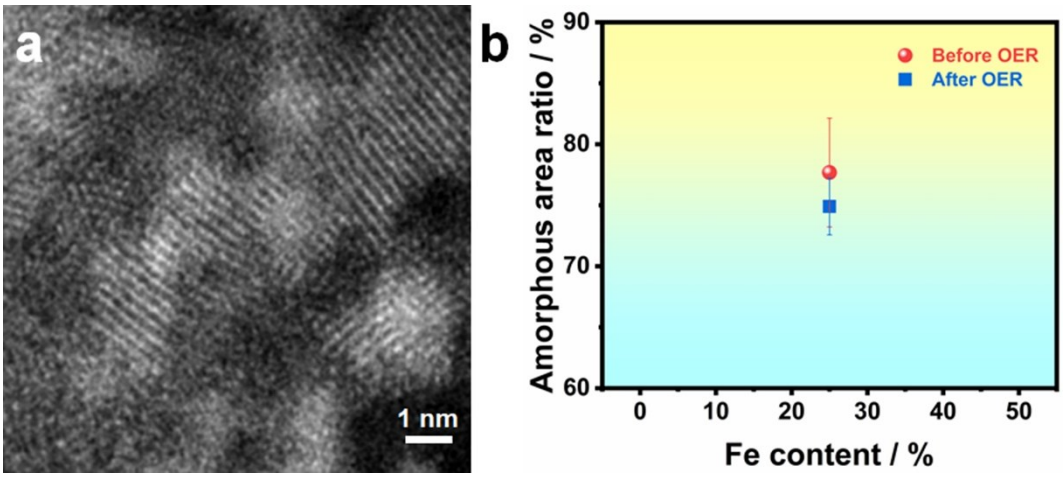


**Fig. S16**. (a) HAADF-STEM image for α-$Ni_{0.75}Fe_{0.25}(OH)_2$ after OER stability test. (b) Amorphous area ratio for α-$Ni_{0.75}Fe_{0.25}(OH)_2$ before and after OER stability test.

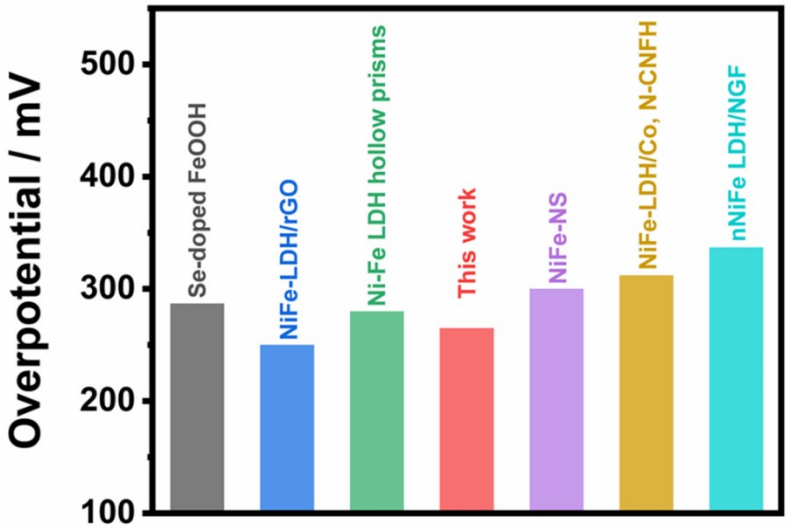


**Fig. S17.** Comparison of the OER catalytic activities for J = 10 mA $cm^{-2}$ of previously reported electrocatalysts.

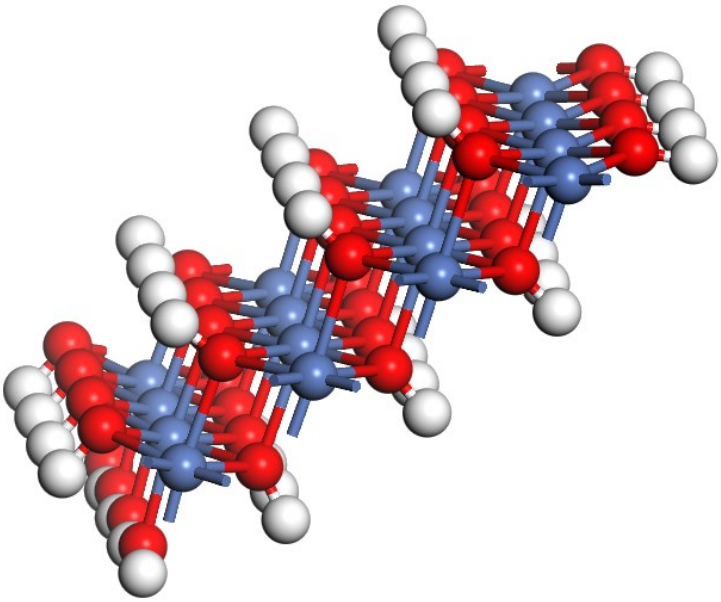

**Fig. S18.** Unoptimized model used for OER calculation. Red: oxygen; blue: nickel; white: hydrogen.

**Table S1.** Reaction conditions for α-$Fe_xNi_y(OH)_2$ nanosheets synthesis, EDS, and ICP results.

| Fe:Ni | Sample | EDS Fe:Ni | ICP Fe:Ni | Ni site (mol) | Fe site (mol) | Total metal site (mol) |
|---|---|---|---|---|---|---|
| 0:1 | α-$Ni(OH)_2$ | 0:1 | 0:1 | $1.95*10^{-7}$ | -- | $1.95*10^{-7}$ |
| 1:9 | α-$Ni_{0.9}Fe_{0.1}(OH)_2$ | 1:7.61 | 1:9.28 | -- | $1.90*10^{-8}$ | $1.90*10^{-8}$ |
| 1:5 | α- | 1:4.85 | 1:4.85 | -- | $2.67*10^{-8}$ | $2.67*10^{-8}$ |
| 1:3 | α- | 1:2.95 | 1:2.89 | -- | $4.35*10^{-8}$ | $4.35*10^{-8}$ |
| 1:2 | α- | 1:2.47 | 1:2.19 | -- | $4.93*10^{-8}$ | $4.93*10^{-8}$ |
| 1:1 | α-$Ni_{0.5}Fe_{0.5}(OH)_2$ | 1:0.45 | 1:0.48 | -- | $1.59*10^{-7}$ | $1.59*10^{-7}$ |

**Table S2.** EIS fitted parameters of samples shown in Figure S8. The equivalent circuit parameters include: The series resistance ($R_s$) between GCE and samples and the charge-transfer resistance ($R_{ct}$) at the working electrode/electrolyte interface.

| | $R_s$ (Ω) | $R_{ct}$ (Ω) |
|---|---|---|
| α-$Ni(OH)_2$ | 10.6 | 145.1 |
| α-$Ni_{0.9}Fe_{0.1}(OH)_2$ | 10.1 | 36.5 |
| α-$Ni_{0.83}Fe_{0.17}(OH)_2$ | 7.4 | 37.94 |
| α-$Ni_{0.75}Fe_{0.25}(OH)_2$ | 10.4 | 17.6 |
| α-$Ni_{0.67}Fe_{0.33}(OH)_2$ | 10.7 | 21.1 |
| α-$Ni_{0.5}Fe_{0.5}(OH)_2$ | 9.6 | 27.6 |
| $RuO_2$ | 10.1 | 87.1 |

**References**


1. A. L. Patterson, *Phys. Rev.*, 1939, **56**, 978-982.
2. B. Mohanty, M. Ghorbani-Asl, S. Kretschmer, A. Ghosh, P. Guha, S. K. Panda, B. Jena, A. V. Krasheninnikov and B. K. Jena, *ACS Catal.*, 2018, **8**, 1683-1689.
3. C. Xia, Q. Jiang, C. Zhao, M. N. Hedhili and H. N. Alshareef, *Adv. Mater.* , 2016, **28**, 77-85.
4. W. Chen, J. Gu, Y. Du, F. Song, F. Bu, J. Li, Y. Yuan, R. Luo, Q. Liu and D. Zhang, *Adv. Funct. Mater.*, 2020, **30**, 2000551.
5. T. Tang, W.-J. Jiang, S. Niu, N. Liu, H. Luo, Q. Zhang, W. Wen, Y.-Y. Chen, L.-B. Huang, F. Gao and J.-S. Hu, *Adv. Funct. Mater.*, 2018, **28**, 1704594.
6. F. Song and X. Hu, *Nat. Commun.*, 2014, **5**, 4477.
7. K. Fan, H. Chen, Y. Ji, H. Huang, P. M. Claesson, Q. Daniel, B. Philippe, H. Rensmo, F. Li, Y. Luo and L. Sun, *Nat. Commun.*, 2016, **7**, 11981.
8. B. Zhang, L. Wang, Z. Cao, S. M. Kozlov, F. P. García de Arquer, C. T. Dinh, J. Li, Z. Wang, X. Zheng, L. Zhang, Y. Wen, O. Voznyy, R. Comin, P. De Luna, T. Regier, W. Bi, E. E. Alp, C.-W. Pao, L. Zheng, Y. Hu, Y. Ji, Y. Li, Y. Zhang, L. Cavallo, H. Peng and E. H. Sargent, *Nat. Catal.*, 2020.
9. S. Lee, L. Bai and X. Hu, *Angew. Chem. Int. Ed.*, 2020, **132**, 8149 –8154.
10. S. Lee, K. Banjac, M. Lingenfelder and X. Hu, *Angew. Chem. Int. Ed.*, 2019, **58**, 10295-10299.